Highly efficient and robust Pt ensembles on mesoporous alumina for reversible H$_2$ charge and release of commercial benzyltoluene molecules

Jinho Oh [a,b], Yeongin Jo [a], Tae Wan Kim [a], Hari Babu Bathula [a,c,1], Sungeun Yang [d], Joon Hyun Baik [e], Young-Woong Suh [a,c,*]

[a] Department of Chemical Engineering, Hanyang University, Seoul 04763, Republic of Korea
[b] Center for Environment & Sustainable Resources Research, Korea Research Institute of Chemical Technology, Daejeon 34114, Republic of Korea
[c] Research Institute of Industrial Science, Hanyang University, Seoul 04763, Republic of Korea
[d] Center for Energy Materials Research, Korea Institute of Science and Technology, Seoul 02792, Republic of Korea
[e] Department of Chemical and Biological Engineering, Sookmyung Women's University, Seoul 04310, Republic of Korea

ARTICLE INFO

ABSTRACT

Metal single atoms often exhibit unique selectivity with maximized atom efficiency. However, they are usually generated at low metal loadings and susceptible to severe reaction conditions resulting in metal sintering, which can be overcome by a new synthesis method offering strong metal–support interaction. Here we show a great potential of one-pot solvent deficient precipitation (SDP) affording mesoporous Pt–Al$_2$O$_3$ (MPtA). This method is unique in creating Pt single atoms and clusters at up to 3 wt% loading because of the restricted Pt mobility by contiguous Al$_2$O$_3$ particles. The MPtA of 3 wt% Pt, representing ensemble species of single atoms and clusters, is more active and stable than the general impregnated catalyst comprised of Pt nanoparticles. Moreover, it successfully accomplishes reversible H$_2$ release and charge of commercial benzyltoluene-type hydrogen carriers. The size and activity of Pt species is readily tuned in the MPtA, which will exert remarkable impacts on catalysis.

1. Introduction

Hydrogen economy will be virtually realized when technological limitations are overcome in the three sectors of H$_2$ production (e.g., grey H$_2$ via steam methane reforming, blue H$_2$ combined with CO$_2$ capture and sequestration, and green H$_2$ via water electrolysis), storage and transportation, and utilization using fuel cells on board and standalone [1–3]. Nowadays, the biggest challenge is to find an economically feasible way of H$_2$ storage and transportation positioned in the middle of the value chain because of low volumetric H$_2$ density [4,5]. Though many options including compressed H$_2$, liquefied hydrogen, physical adsorption in nanoporous materials, metal hydrides, etc. are being studied, a great deal of attention has been paid to chemical hydrogen storage based on liquid organic hydrogen carriers (LOHC) because it appears more fit to massive storage and overseas transportation [6–9]. The LOHC concept is, simply speaking, to reversibly interconvert H$_2$-lean and H$_2$-rich molecules by catalytic hydrogenation (H$_2$ charge) and dehydrogenation (H$_2$ release) [10–12]. The reported LOHC molecules can be categorized into two classes according to the presence of

heteroatoms. The typical aromatic examples are toluene and heat transfer oils [13], such as monobenzyltoluenes (MBT) and dibenzyltoluenes (DBT) [14,15], while the heteroaromatic ones are N-ethyl-carbazole (NEC) and 2-(n-methylbenzyl)pyridine (MBP) [16,17]. Each class has pros and cons, yet the universal requirement for their successful implementation is a dehydrogenation catalyst of high efficiency under mild conditions and robustness in successive uses, which will be embedded in traditional or state-of-the-art catalytic reactors [18]. Moreover, it is ideal if the same catalyst achieves full conversion at a higher rate in the hydrogenation reaction.

Among a variety of dehydrogenation catalysts, platinum (Pt) and palladium (Pd) are recognized as the most powerful metal in H$_2$ release from cyclic and heterocyclic LOHC molecules, respectively. First, Pd is examined to be more active than Pt in most of N-containing LOHC molecules such as NEC, MBP, and alkylindoles, because of strong ability of metallic Pd to adsorb N atom of the tested substrate [19]. Generally, the important properties of Pd catalysts affecting the dehydrogenation activity are Pd dispersion, Pd–support interaction, and surface fraction of active Pd (111) plane in supported Pd nanoparticles [20]. These were

all accomplished by the mesoporous Pd–Al$_2$O$_3$ (MPdA) generated by solvent deficient precipitation (SDP) [21,22]. This method offers high surface area and mesoporosity without the use of structure directing agents. The MPdA of 1 wt% Pd afforded the improved dehydrogenation capability and negligible activity loss compared to the impregnated catalyst Pd/Al$_2$O$_3$ for N-heterocyclic molecules. This superior performance was attributed to highly dispersed Pd particles with a pronounced population of (111) plane, provided by the unique SDP environment to prevent Pd particles adjacent to alumina from being sintered.

In the case of cyclic LOHC molecules, Pt is capable of excellently rupturing C–H bonds [23]. However, the catalytic functions necessary for Pt-based catalysts should be well controlled because higher temperatures are demanded due to the higher dehydrogenation enthalpy than heterocyclic molecules [13,24]. Under this circumstance Pt works actively in the cleavage of C–C bonds, thereby giving rise to cracking products including small alkanes and aromatics [25,26]. Thus, various approaches have been taken, such as tuning the size and surface plane of Pt particles [27,28], modifying surface functionality of supports [15], and adding metal promoters [29], all of which are ultimately directed toward achieving the maximum efficiency of Pt atom, reducing defect-induced side reactions, and maintaining the fresh catalyst state. In this regard, the most straightforward solution is to discover such a new synthesis method that can acquire these at the same time. Therefore, the simple, cost-effective SDP method is worthwhile being explored for supported Pt catalysts, as exemplified in the MPdA catalyst.

Here we report a great potential of the mesoporous Pt–Al$_2$O$_3$ (MPtA) synthesized by the SDP method in reversible H$_2$ release and charge of commercial benzyltoluene-based LOHC molecules such as MBT and DBT. The MPtA exhibits extremely high performance in both the dehydrogenation and hydrogenation reactions, and is amazingly robust in successive H$_2$ storage–release cycles, compared to the conventional impregnated Pt counterpart. Furthermore, the SDP method predominantly yields Pt single atoms and clusters even at higher Pt loadings, unlike the general methods producing single atoms at the Pt content of less than 1 wt% [30–32]. As a result of finding an optimal Pt loading, the ensemble comprised of Pt single atoms and clusters is verified to be accountable in both the superior H$_2$ storage and release capabilities of the MPtA at 3 wt% Pt. This is further confirmed by the activities of the control samples prepared under different calcination conditions. Through spectroscopic characterizations and H$_2$ desorption experiments, the strong interaction between Pt and Al$_2$O$_3$ governs the characteristics, (de)hydrogenation performance, and durability of the MPtA catalyst.

2. Experimental

2.1. Preparation of supported Pt catalysts

The MPtA catalysts were intended to synthesize about 3 g (based on the weight of reduced catalyst) at a single batch. Typically, Pt (NH$_3$)$_4$(NO$_3$)$_2$ (0.06–0.30 g), Al(NO$_3$)$_3$.9 H$_2$O (21.4–22.3 g), and NH$_4$HCO$_3$ (13.65–14.10 g) were placed in a mortar without solvent. Note that the mole ratio of total nitrate to bicarbonate was set at 1.0. Then, the solid mixture was ground with a pestle for twenty min at room temperature. The prepared wet solid was calcined at 600 °C for 5 h (ramping: 2 °C min^{-1} to 600 °C) and then reduced by pure H$_2$ at 500 °C for 3 h (ramping: 5 °C min^{-1} to 500 °C). The samples are named MxPtA with x of 1, 2, 3, and 5 in a unit of wt% Pt.

For comparison, Pt/γ-Al$_2$O$_3$ (Pt/gA) were prepared by impregnating a certain volume of aqueous Pt(NH$_3$)$_4$(NO$_3$)$_2$ solution onto γ-Al$_2$O$_3$ (STREM) and drying at 105 °C in a static oven. The final Pt/gA catalysts were obtained by the same thermal treatment as for the MPtA. The samples are named xPt/gA with x of 1, 2, 3, and 5 in a unit of wt% Pt.

2.2. Activity tests for dehydrogenation and hydrogenation reactions

Experiments for the dehydrogenation of H$_{12}$-MBT proceeded in a batch reactor with the internal volume of 90 cm^3. After the catalyst was pre-loaded to the reactor vessel, H$_{12}$-MBT (7.3 mmol) was added dropwise, where the mole ratio of Pt to H$_{12}$-MBT varied to a desired level, and oxygen and moisture in the internal of the reactor were removed by purging with N$_2$ for 10 min. Then, the reactor was heated to a desired temperature using a commercial Marlotherm SH at a ramping rate of 18 °C min^{-1}. While the reaction progressed for a desired duration, the quantity of H$_2$ released from the reactant was measured by the volume of water displaced in a burette. After completion, the reactor was cooled to ambient temperature. Finally, the dehydrogenation product mixture was filtered using a syringe filter (0.1 μm).

For the hydrogenation reaction, H$_0$-MBT (15 cm^3) and Pt catalyst were added into an autoclave reactor (internal volume: 150 cm^3) with a glass liner, where the molar ratio of Pt relative to the initial H$_0$-MBT varied. Then, N$_2$ purging was conducted before reaction, followed by pressurizing with 99.9% H$_2$ to a desired pressure that was maintained throughout the reaction. When the reaction mixture reached 150 °C, the hydrogenation reaction was started together with the stirring of 400 rpm. After the reaction for a certain duration, the reactor was cooled to room temperature. Then, the catalyst solid was separated from the hydrogenation product mixture via a syringe filter (0.1 μm).

To test reversibility for hydrogenation and dehydrogenation, a mixture containing H$_0$-MBT (10 g, 51.5 mmol) and 3 wt% Pt catalysts (0.4 mol% Pt/H$_0$-MBT) was loaded into a 150 ml stainless steel autoclave reactor. After N$_2$ purging to remove oxygen and moisture inside, the reactor was flushed with hydrogen (99.9%) and pressurized to 35 bar. Then, the reactor was heated to 150 °C and maintained for 2 h. After cooling to room temperature, a small aliquot of the product mixture was taken for quantitative analysis. For the next dehydrogenation reaction, the valve of vent line was opened to atmosphere pressure (1 bar) without any treatment. Then, the reactor was immediately heated to 250 °C. After the dehydrogenation of the hydrogenated product mixture for 4 h, the temperature was decreased to room temperature and then a small liquid sample was taken. Such a hydrogenation–dehydrogenation cycle was repeated twice more in a consecutive way. The catalytic performance in H$_2$ uptake and release was calculated by analyzing the product samples taken after each reaction.

2.3. Product analysis

The product mixture (ca. 1.5 g) obtained after the above experiments, was diluted with acetone (20 cm^3) and mixed with nonane as a calibration solvent for product analysis. This sample was analyzed in a Younglin YL6500 gas chromatograph (GC) with a flame ionization detector (FID) and a HP-5 column (30 m × 0.32 mm× 0.25 μm). To double check the reproducibility of GC analysis, an Agilent Technologies 7890 A GC with a Restek Rxi®− 17Sil column (30 m × 0.25 mm × 0.25 μm) and an auto sampler (7683D) was additionally used. In both the hydrogenation and dehydrogenation reactions, the calculation of reactant conversion and product selectivities was based on the protocol employed in our previous study [33].

In all experiments, only the reaction intermediate H$_6$-MBT was observed except the target products (H$_0$-MBT in dehydrogenation and H$_{12}$-MBT in hydrogenation) at complete conversion. In case of dehydrogenation products, no other gases except H$_2$ were detected and the liquid-phase products contained only H$_0$-, H$_6$-, and H$_{12}$-MBT without byproducts. Also, unknown products were not formed in the hydrogenation reaction. Hence, the selectivities of H$_6$-MBT and the target product were summed up close to 100% in all reaction runs. The product selectivities are provided in Supplementary Information.

2.4. Catalyst characterization

The textural properties of the supports and Pt catalysts were measured in a Micromeritics 3Flex after the sample (0.1 g) was preliminary evacuated at 200 °C for 2 h. Pt loading in the prepared Pt catalysts was measured with an inductively coupled plasma optical emission spectrometer (ICP-OES) using an OPTIMA 8300 (Perkin Elmer). The crystallinity of powder samples was measured by X-ray diffraction (XRD) analysis using a Rigaku miniFlex300 diffractometer with a Cu Kα radiation source of 30 kV and 10 mA, where all of the XRD patterns were recorded in the 2θ range of 10°–80° at a rate of 4° min^{-1} and a step of 0.02°. Pt size and distribution were characterized by high angle annular dark field scanning transmission electron microscope (HAADF-STEM) in a Titan cubed G2 60-300 (FEI) with a high operating voltage of 300 kV. Prior to the analysis, a catalyst sample suspended in methanol was loaded onto a copper grid, followed by subsequent drying at 60 °C in vacuum.

Experiments for temperature programmed desorption of hydrogen (H$_2$-TPD) were conducted with a Micromeritics AutoChemII 2910 equipped with a thermal conductivity detector (TCD). After a pre-reduced sample (60 mg) was pretreated under argon at 200 °C for 1 h, the reactor was cooled to 40 °C. Then, the sample was exposed to a flow of 10% H$_2$/Ar (50 cm^3 min^{-1}) during 1 h. As soon as an argon purge (30 cm^3 min^{-1}) for 30 min was finished, H$_2$ desorption was started as the temperature increased at a rate of 10 °C min^{-1} to 900 °C.

Experiments of CO chemisorption was performed using a BELCAT-B instrument (BEL Japan, Inc.) to measure the dispersion of Pt nanoparticles. After a sample (50 mg) was reduced at 350 °C for 3 h in a flow of 10% H$_2$ in argon (30 cm^3 min^{-1}) and then cooled to 30 °C in a flow of helium (30 cm^3 min^{-1}), a pulse injection of 5% CO gas in He was repeated until the area of CO peak became saturated. The adsorbed quantity of CO was determined by integrating all of the peak areas obtained until saturation and comparing with the area corresponding to the total amount of CO injected via a sample loop. Pt dispersion was calculated from the assumption that the CO/Pt mole ratio is 1:1. Additionally, diffuse reflectance infrared Fourier transform (DRIFT) spectroscopy was performed for distinguishing the chemisorbed CO species. Prior to measurement, a powder sample (30 mg) in a Harrick Praying Mantis high temperature reaction chamber installed with a Nicolet 6700 FT-IR was reduced at 500 °C for 1 h in a flow of 5% H$_2$ in argon (100 cm^3 min^{-1}). After cooling to 50 °C, inert N$_2$ was supplied for 1 h to remove physisorbed H$_2$ molecules and then a background spectrum was obtained. Finally, a spectrum of CO-chemisorbed sample was taken after feeding a flow of 5% CO in agron (50 cm^3 min^{-1}) for 30 min and subsequent evacuation for 30 min. X-ray absorption spectroscopy (XAS) was performed at the 8 C and 10 C beamlines of the Pohang Light Source (PLS). The beam energy and current of the storage ring electron are 3.0 GeV and 300 mA, respectively. A Si(111) double crystal was used as a monochromator that was detuned by 30% to minimize unwanted harmonics. Pt L3 edge spectra were acquired with a passivated implanted planar Si detector (Canberra) in a fluorescence mode. Pt foil and PtO$_2$ (Sigma-Aldrich) were measured as a reference for Pt metal and oxide, respectively. The ATHENA and ARTEMIS programs were used for processing and fitting the measured XAS spectra. The reported coordination numbers were calculated using the S02 values determined by fitting the reference samples Pt foil and PtO$_2$. The Debye−Waller factors (σ^2) were reasonably fixed when the number of independent points was limited.

3. Results and discussion

3.1. Dehydrogenation performance of mesoporous Pt–Al$_2$O$_3$

For the MPtA and Pt/gA catalysts with the nominal Pt loading of 3 wt % (M3PtA and 3Pt/gA, respectively), the results of ICP-OES analysis showed that the actual Pt loading was similar each other at 2.9 ± 0.02 (Table 1). N$_2$ physisorption measurement examined that the specific surface area (347 m^2 g^{-1}) and pore volume (0.57 cm^3 g^{-1}) of mesoporous alumina (m-Al$_2$O$_3$) were larger than those of γ-Al$_2$O$_3$. This difference was similarly observed in the fresh M3PtA and 3Pt/gA (Table 1). A higher level of mesoporosity is generated by the SDP method irrespective of Pt addition. While the hysteresis loops in the isotherms of the two samples look alike (Fig. S1), the pore size distribution of the fresh M3PtA is narrow and centered at the diameter of around 50 Å, much different from that of the fresh 3Pt/gA, which explains more regularity of mesopores in the former sample.

The two catalysts were tested for H$_2$ release from H$_{12}$-MBT, where the reaction temperature and mole ratio Pt/H$_{12}$-MBT varied. The detailed results are presented in Table S1. At the temperatures of 230–270 °C, M3PtA showed the higher H$_2$ yield (calculated by both the GC results of the liquid product and measured gas volumes) by 7–30% than 3Pt/gA (Fig. 1a). Outstandingly, the activity of M3PtA at 250 °C was nearly equivalent to that of 3Pt/gA at 270 °C and the efficiency of M3PtA at the low temperature of 230 °C was even higher than when a 3-fold larger amount of 3Pt/gA was used. Moreover, H$_2$ productivity (calculated at the dehydrogenation degree of 50%) was 3.9- and 2,7-fold higher with M3PtA (354 and 423 mmol$_{H2}$ g$_{Pt}^{-1}$ min^{-1}) than with 3Pt/gA (90 and 154 mmol$_{H2}$ g$_{Pt}^{-1}$ min^{-1}) at 250 and 270 °C, respectively. Since the decrease in H$_2$ productivity with reaction temperature is much lower with M3PtA than 3Pt/gA, the adsorption and persistence of dehydrogenation products (H$_6$-MBT and H$_0$-MBT) are presumed to be lower on M3PtA than on 3Pt/gA. The superior performance of M3PtA was confirmed in the dehydrogenation of H$_{18}$-DBT at 270–310 °C, where higher temperatures were employed because of the higher reaction enthalpy for H$_{18}$-DBT [34]. As presented in Fig. 1b and Table S2, M3PtA released 1.4–1.8 fold larger H$_2$ volume than 3Pt/gA. The initial reaction rate at the identical temperatures also appeared to be higher with M3PtA, as observed in H$_{12}$-MBT dehydrogenation. The activation energy (E_a), calculated from the rate constants obtained in initial H$_2$ release curves, for both H$_{12}$-MBT and H$_{18}$-DBT were lower by ca. 25 kJ mol^{-1} with M3PtA than 3Pt/gA (Fig. 1c). This excellent performance of M3PtA is explained by the much higher Pt dispersion compared to 3Pt/gA.

Catalyst stability was examined in the dehydrogenation of H$_{12}$-MBT at 250 °C and 0.1 mol% Pt/H$_{12}$-MBT. As a result of recycling both catalysts five times, M3PtA preserved the initial H$_2$ yield at ca. 81–82% whereas 3Pt/gA showed the continuous decrease in H$_2$ yield from 56%

Table 1
Properties of the alumina supports and Pt catalysts with the nominal Pt loading of 3 wt%.

Sample	Actual Pt content [wt%][a]	Surface area [m^2 g^{-1}][b]	Pore volume [cm^3 g^{-1}][b]	Avg. pore size [Å][b]	Pt dispersion [%][c]
γ-Al$_2$O$_3$	–	169	0.41	97.4	–
m-Al$_2$O$_3$	–	347	0.57	41.0	–
Fresh 3Pt/gA	2.88	164	0.37	89.1	41.9
Fresh M3PtA	2.92	319	0.50	49.5	92.4
Spent 3Pt/gA	2.72	140	0.39	81.7	4.9
Spent M3PtA	2.89	314	0.48	49.2	92.0

[a] Measured by ICP-OES analysis.
[b] Measured by N$_2$ physisorption, where the average pore diameter was calculated from the results in the desorption.
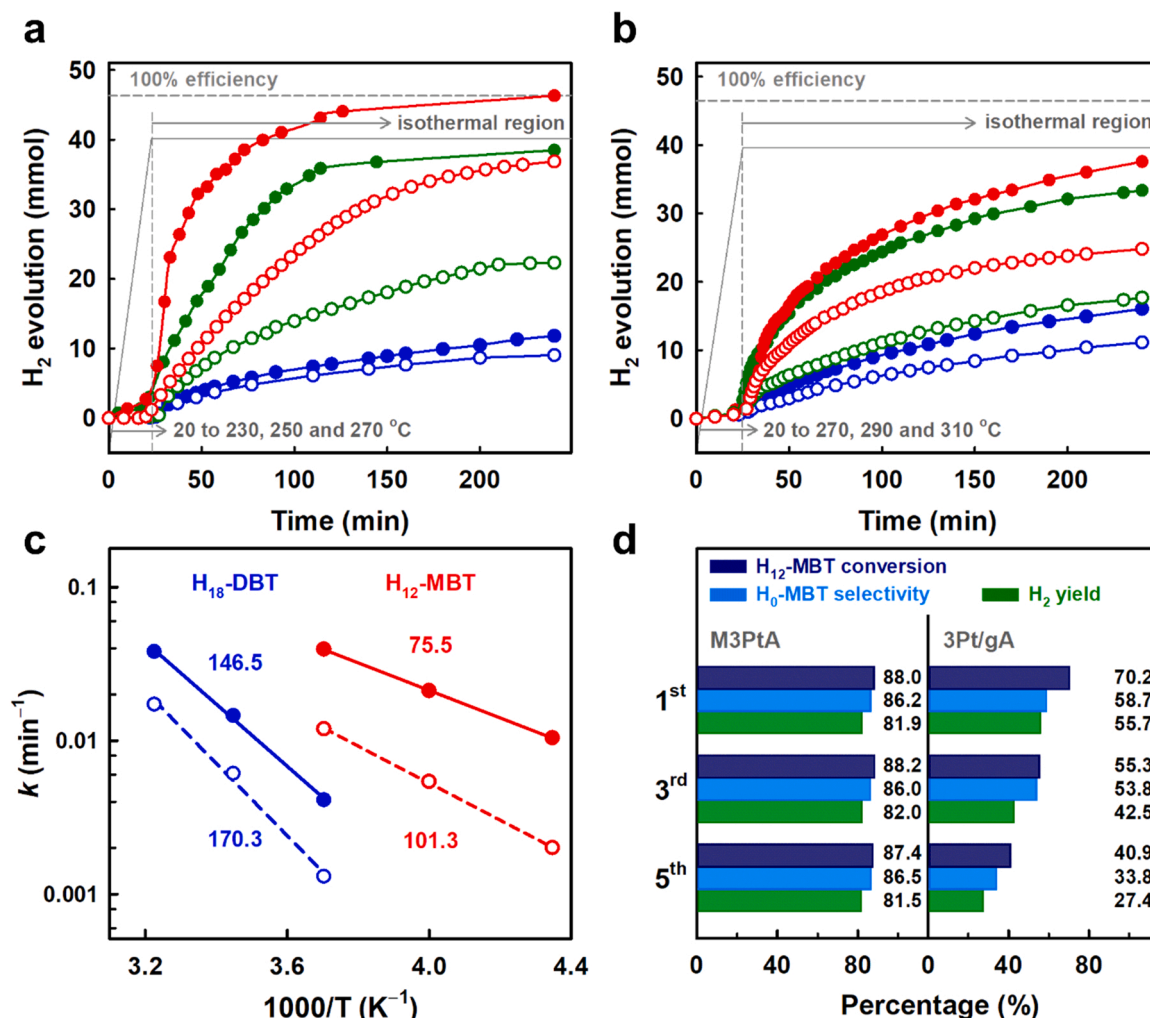[c] Measured by CO chemisorption.

Fig. 1. Dehydrogenation activity and stability of M3PtA (filled symbols) and 3Pt/gA (open symbols). (a) H_2 evolution curves from H_{12}-MBT at 230 (blue), 250 (green), and 270 (red) °C with 0.1 mol% Pt/H_{12}-MBT for 4 h. (b) H_2 evolution curves from H_{18}-DBT at 270 (blue), 290 (green), and 310 (red) °C with 0.75 mol% Pt/ H_{12}-MBT for 4 h. (c) Arrhenius plots to calculate the activation energy (E_a in a unit of kJ mol^{-1}) for H_{12}-MBT (red) and H_{18}-DBT (blue). (d) Catalyst reusability in the dehydrogenation of H_{12}-MBT at 0.1 mol% Pt/H_{12}-MBT and 250 °C for 4 h, where the number of catalyst use is represented in the left-hand side. (For interpretation of the references to colour in this figure legend, the reader is referred to the web version of this article.)

to 27% (Fig. 1d and Table S3). Moreover, the selectivity of the full dehydrogenation product H_0-MBT was maintained at 86% in all recycle runs over M3PtA, different from the decrease in H_0-MBT selectivity over 3Pt/gA. It should be noted here that the other product is only the intermediate H_6-MBT without any missing products. The Pt loading was nearly the same between the fresh and spent 3Pt/gA, and the textural properties were not considerably changed (Table 1). The outstanding difference was observed in the HAADF-STEM images and XRD patterns of the spent catalysts: the growth of Pt nanoparticles was evident in 3Pt/ gA (Fig. S2). This indicates that, unlike the impregnated Pt/gA, Pt mobility in the MPtA is inhibited by neighboring Al_2O_3 particles, as in the MPdA [21,22], hence keeping the dehydrogenation activity in repeated use.

3.2. Hydrogenation performance of mesoporous Pt–Al_2O_3

The hydrogenation of H_0-MBT over M3PtA and 3Pt/gA were performed at 35 bar H_2 and 0.1 mol% Pt/H_0-MBT for 2 h (Table S4). The tests at 110, 130, and 150 °C examined the superior H_2 storage efficiency of M3PtA to 3Pt/gA; particularly, the activity at 110 °C was 2-fold higher with M3PtA (Fig. 2a). Similar to H_2 productivity in the dehydrogenation reaction, H_2 charge rates were calculated. At the hydrogenation degree of 10%, M3PtA exhibited 808, 1178, and

1801 mmol$_{H2}$ g$_{Pt}^{-1}$ min^{-1} at 110, 130, and 150 °C, respectively. When compared to the H_2 charge rates of 3Pt/gA (468, 936, and 1705 at 110, 130, and 150 °C, respectively), the rate difference between each other is larger as the reaction temperature decreases. This implies that the reactant H_0-MBT is more strongly adsorbed on the surface of M3PtA. The similarity was also found at 15% hydrogenation degree. Moreover, H_{12}-MBT was more selectively formed over M3PtA at all the temperatures (> 95%), indicating that the intermediate H_6-MBT (formed by preferential hydrogenation of benzene ring) is hydrogenated at a faster rate over M3PtA than over 3Pt/gA.

When H_2 consumption was measured using a high-pressure gas burette in the hydrogenation of H_0-DBT at 50 bar H_2, 150–170 °C, and 0.06 mol% Pt/H_0-DBT (Fig. 2b), H_2 storage was much faster with M3PtA than with 3Pt/gA at the identical temperatures: for instance, H_2 charge at 150 °C was full within 70 min with M3PtA that was over 2-fold shorter with 3Pt/gA (156 min). As assessed in the dehydrogenation experiments, the first-order rate constants were obtained in H_0-MBT dehydrogenation (Fig. S3). The calculated E_a value from the Arrhenius plot was 28.1 kJ mol^{-1} for M3PtA much smaller than 47.4 kJ mol^{-1} for 3Pt/gA (Fig. 2c), which is caused by the high Pt dispersion of M3PtA along with easy pore diffusion owing to mesoporosity. This was similarly found in H_0-DBT hydrogenation, though the difference was reduced because of high temperatures. Through additional experiments to vary
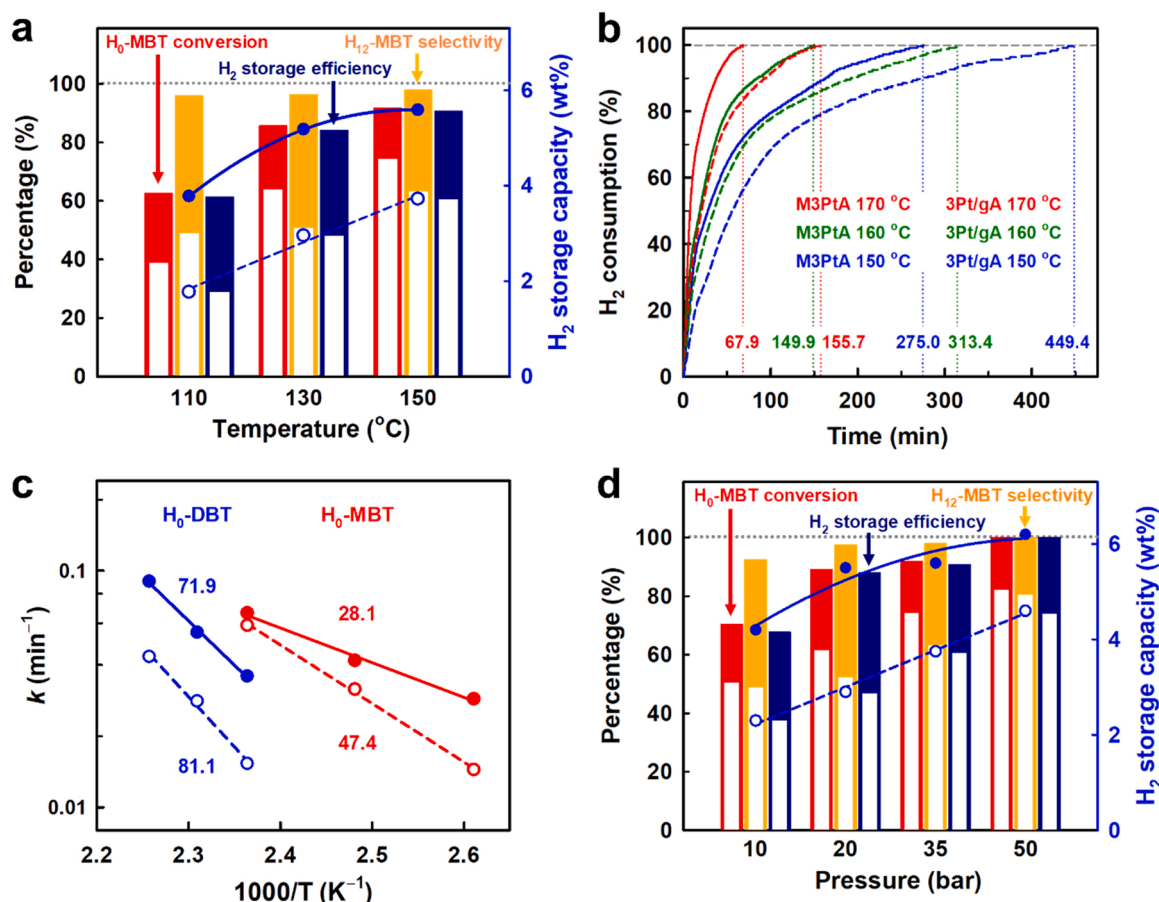
Fig. 2. Hydrogenation activity of M3PtA (filled bars/symbols and solid lines) and 3Pt/gA (blank bars/symbols and dashed lines). (a) Activity results for H_0-MBT at 110–150 °C, 0.1 mol% Pt/H_0-MBT, 35 bar H_2, and 2 h. (b) H_2 consumption curves from H_0-DBT at 150 (blue), 160 (green), and 170 (red) °C, 50 bar H_2, and 0.06 mol% Pt/H_0-DBT. The value in the panel represents the time for full H_2 charge. (c) Arrhenius plots to calculate the activation energy (E_a) for H_0-MBT (red) and H_0-DBT (blue). (d) Effect of H_2 pressure on the hydrogenation activity for H_0-MBT at 150 °C, 0.1 mol% Pt/H_0-MBT, and 2 h.(For interpretation of the references to colour in this figure legend, the reader is referred to the web version of this article.)

H_2 pressure from 10 to 50 bar, the superior H_2 storage efficiency was attained with M3PtA even at low pressures, along with the H_{12}-MBT selectivity of above 90% without side products formed by cracking (Fig. 2d and Table S5). It is worth noting that the hydrogenation of H_0-MBT over M3PtA was complete at 50 bar H_2, 150 °C, 0.1 mol% Pt/H_0-MBT, and 2 h.

3.3. Reversible H_2 charge and release over mesoporous Pt–Al_2O_3

The above results manifest that M3PtA can release and store H_2 efficiently for benzyltoluene molecules. According to the report of Shi et al. [35], a couple of H_0-MBT hydrogenation and H_{12}-MBT dehydrogenation were repeatedly performed in a batch reactor. Fig. 3 displays the activity results in the three cycles of interconversion along with a
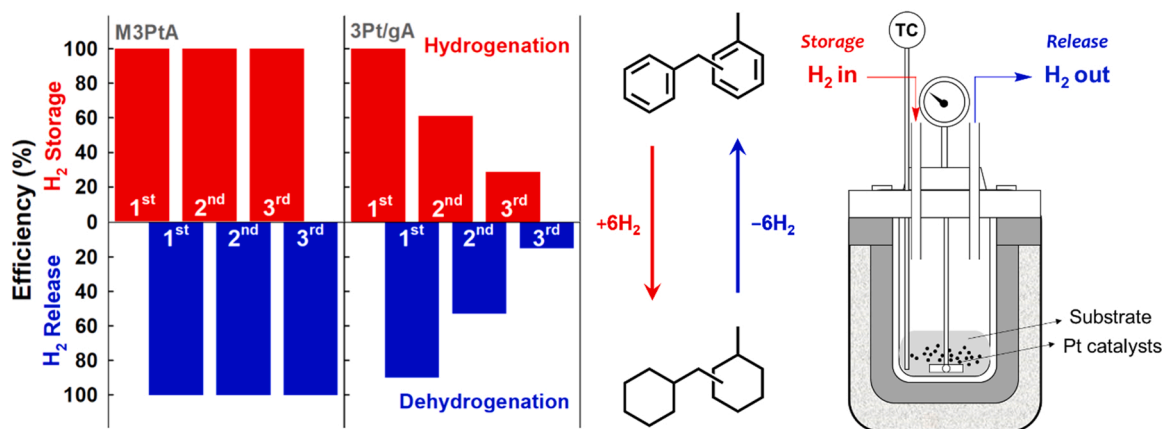

Fig. 3. Catalyst reversibility of M3PtA and 3Pt/gA in H_2 charge and release using a single reactor initially charged with 0.4 mol% Pt/H_0-MBT. Reaction conditions: (hydrogenation) 150 °C, 35 bar H_2, and 2 h; (dehydrogenation) 250 °C and 4 h.

schematic of the reactor (detailed results in Table S6). From preliminary results, the mole ratio Pt/H_0-MBT was set at 0.4 mol% for the reversibility test. The first H_2 charge into H_0-MBT at 150 °C and 35 bar H_2 for 2 h was perfect over both M3PtA and 3Pt/gA. When the next dehydrogenation of H_{12}-MBT was performed at 250 °C for 4 h using the same reaction apparatus without catalyst replacement and activation, the H_2 yield remained 100% with M3PtA but it was lowered to 90 mol% with 3Pt/gA. In the next two cycles, the catalytic performance of M3PtA was maintained. However, the hydrogenation and dehydrogenation activities of 3Pt/gA were continuously declined and finally, the H_2 yield was only 15 mol%. This highlights the reusability of M3PtA without activity loss in consecutive H_2 charge–release cycles, as similar to the consecutive dehydrogenation cycles with M3PtA.

3.4. Effect of Pt loading on the H_2 release and charge performance of mesoporous Pt–Al_2O_3

The dispersion of supported Pt particles is often affected by Pt loading [36]. Thus, the MPtA and Pt/gA of three different Pt loadings (MxPtA and xPt/gA with x = 1, 2, and 5 in a unit of wt%) were prepared, where their properties are listed in Table S7. The performance of these catalysts along with M3PtA and 3Pt/gA was evaluated in both H_{12}-MBT dehydrogenation and H_0-MBT hydrogenation (detailed results in Tables S8 and S9). In the dehydrogenation of H_{12}-MBT, the conversion, H_0-MBT selectivity, and H_2 yield over MxPtA interestingly showed a volcano-shaped relationship with the Pt loading, where the maximum was achieved with M3PtA and the minimum with M1PtA (Fig. 4a). In contrast, 1Pt/gA exhibited the best performance among xPt/gA and H_2 storage capacity was descending with the Pt loading.

The similar trends of MxPtA and xPt/gA with the Pt loading were observed in H_0-MBT hydrogenation. In detail, H_2 storage efficiency of MxPtA was the highest with 3 wt% Pt and the lowest with 1 wt% Pt, whereas that of xPt/gA decreased with the increase in Pt loading (Fig. 4b). A more interesting finding was noticed when comparing the activities at the same Pt loading: 1Pt/gA is superior to M1PtA in both reactions, whereas MxPtA are more active than xPt/gA at the other Pt loadings.

The above results suggest that the SDP method produces Pt species of different sizes and/or characters from the general impregnation method. Thus, HAADF-STEM images of MxPtA and xPt/gA catalysts were compared (Fig. 5). In the image of 1Pt/gA, various sizes of Pt particles are visible: single atoms, clusters (loose packing with longer interatomic distances than nanoparticles) [37–39], and crystalline nanoparticles. The crystallinity of Pt particles in 1Pt/gA was confirmed by the XRD reflections of Pt (111), (200), and (220) planes, which was also seen in the other xPt/gA (Fig. S4). As the Pt loading increases from 2 to 5 wt%, Pt single atoms are less popular whereas Pt nanoparticles are more abundant and larger, consistent to more intense Pt reflections in their XRD patterns. The growth of Pt particles in the Pt/gA clearly explains the linearly descending activity trends in both H_{12}-MBT dehydrogenation and H_0-MBT hydrogenation, because surface Pt atoms are less available as larger Pt nanoparticles are formed.

In sharp contrast, the MPtA catalysts display very different Pt species with the Pt loading (upper row in Fig. 5). Most of Pt species in M1PtA are single atoms, which is fascinating because conventional impregnation rarely affords metal single atoms at 1 wt% loading. Even in the micrographs of M2PtA and M3PtA, Pt single atoms are still dominant. Moreover, Pt clusters appear in M2PtA and M3PtA. In the XRD patterns of MxPtA, the reflection of Pt (111) was only apparent for M5PtA though much less than all of the xPt/gA (Fig. S4). When compared with the activity results in H_2 release and storage, the HAADF-STEM images of MxPtA suggest that Pt ensembles (comprised of Pt single atoms and clusters) are more catalytically superior to Pt single atoms alone and Pt nanoparticles of higher densities as well. The similarity was identified in the magnetite-supported Pd clusters tested in the hydrogenation of various alkene substrates, where Pd clusters with best activity were
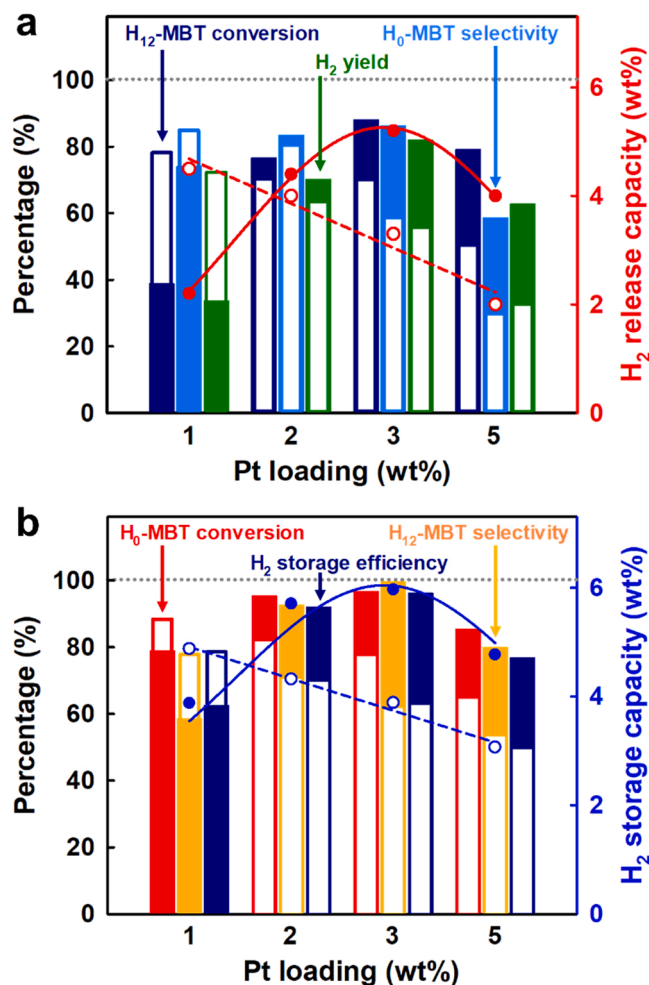

Fig. 4. Dependence of Pt loading on catalytic activities of the MxPtA (filled bars and symbols) and xPt/gA (blank bars and symbols). (a) Catalytic performance in the dehydrogenation of H_{12}-MBT at 250 °C, 0.1 mol% Pt/H_{12}-MBT, and 4 h. (b) Catalytic performance in the hydrogenation of H_0-MBT at 150 °C, 35 bar H_2, 0.22 mol% Pt/H_0-MBT, and 2 h. H_2 release and storage capacities are calculated using the theoretical H_2 storage density of 6.15 wt%.

obtained at 0.38 wt% Pd [40]. This loading is substantially lower than the Pt loadings found in this work, M2PtA and M3PtA. Therefore, the SDP method offers a broad range of Pt loading in synthesizing single atoms and clusters simultaneously.

3.5. Tuning the size of Pt nanoparticles in mesoporous Pt–Al_2O_3

To confirm the aforementioned effects of Pt loading, the control samples were prepared by employing harsher conditions than the original one (ramping at 2 °C min^{-1} to 600 °C and maintaining for 5 h). From preliminary tests, the calcination duration was changed to 40 h with the others fixed (denoted as B1) and in another way, the ramping rate only varied to 10 °C min^{-1} (named B2). The variations were mainly applied for M1PtA and M3PtA to change their catalytic performance to large extents. The properties of these size-controlled Pt catalysts are presented in Table S10.

For M1PtA, the changes in calcination duration and ramping rate are successful in the formation of Pt clusters, as seen in the HAADF-STEM images of M1PtA_B1 and M1PtA_B2 (Fig. 6a). This increase in Pt size contributed to activity enhancement of M1PtA in H_{12}-MBT dehydrogenation (Fig. 6b and Table S11) and H_0-MBT hydrogenation (Fig. 6c). Also, the inferior activities of M1PtA_B2 to M1PtA_B1 in both reactions are explained by the formation of crystalline Pt nanoparticles in the
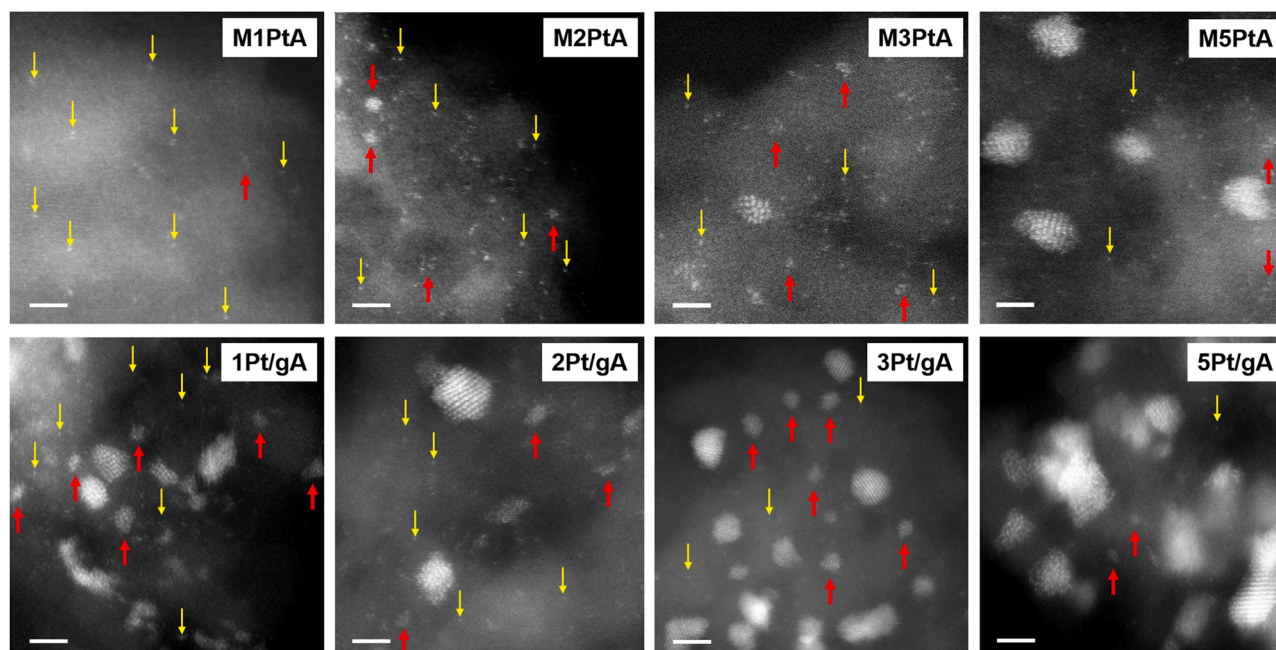
Fig. 5. HAADF-STEM images of the M*x*PtA and *x*Pt/gA with the Pt loading (*x*) of 1, 2, 3, and 5 in a unit of wt%. The yellow and red arrows mark Pt single atoms and clusters, respectively. Scale bar = 2 nm.
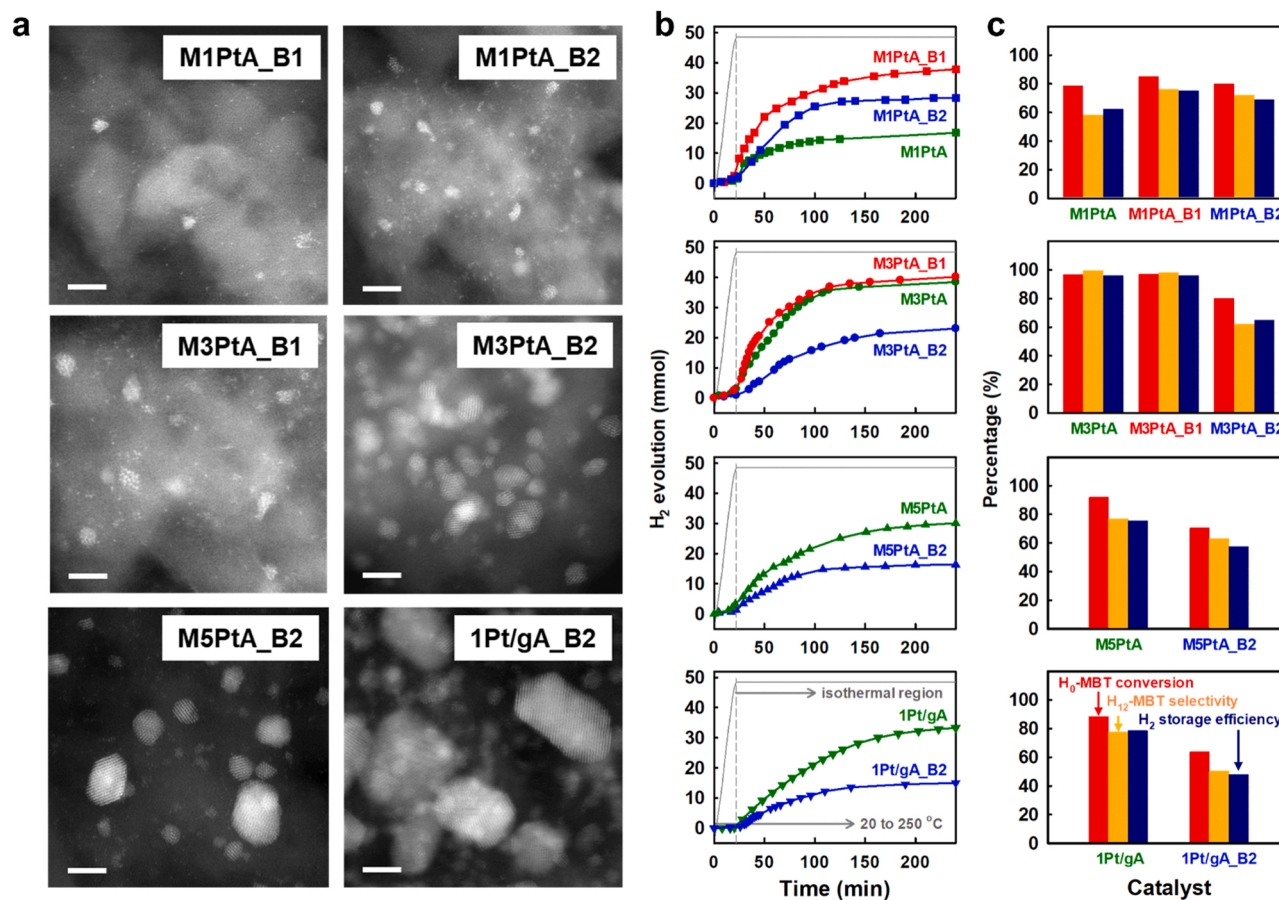

Fig. 6. Pt nanoparticles and activities of the size-controlled Pt catalysts (M*x*PtA and *x*Pt/gA with *x* = 1, 3, and 5 in a unit of wt%). (a) HAADF-STEM images. Scale bar = 2 nm. (b) H$_2$ release curves in the dehydrogenation of H$_{12}$-MBT. Reaction conditions: 250 °C, 0.1 mol% M/R, 4 h. (c) Catalytic performance in the hydrogenation of H$_0$-MBT. Reaction conditions: 150 °C, 35 bar, 0.22 mol% M/R, 2 h. B1 and B2 represent the changes in the calcination duration from 5 to 40 h and the ramping rate from 2° to 10°C min^{-1}, respectively.

former catalyst examined by the Pt (111) reflection in the XRD pattern (Fig. S5a). When the calcination condition varied for M3PtA, more clear features were found. First, M3PtA_B1 was comparable to M3PtA in both reactions, meaning that the longer calcination does not induce significant change in the Pt species of M3PtA. However, M3PtA_B2 shows the growth of Pt nanoparticles, resulting in the much reduced dehydrogenation and hydrogenation activities compared to M3PtA. The similar effects were observed in between M5PtA and M5PtA_B2 and between 1Pt/gA and 1Pt/gA_B2. The ramping rate in calcination, therefore, is a crucial parameter in tuning the Pt size in the MPtA. Consequently, Pt ensembles indeed exhibit the best catalytic performance in H_2 release and storage of benzyltoluene molecules.

3.6. Chemical features of mesoporous Pt–Al₂O₃

The local atomic structure of Pt in M*x*PtA and *x*Pt/gA was studied using the extended X-ray absorption fine structure (EXAFS) region of XAS spectra (Fig. 7). For all Pt/gA catalysts, the k^3-weighted EXAFS spectra at the L_3-edge of Pt resemble each other, where the Pt–Pt contribution at 2.7 Å is the major based on the reference Pt foil. With the Pt loading increasing, the Pt–O contribution becomes a little smaller. Calculated from the fitting results (Table S12), the Pt–Pt coordination number (CN) is 6.9 ± 0.6 for 5Pt/gA, explaining the increased size of Pt nanoparticles with the disappearance of single atoms and clusters. The EXAFS spectra of M*x*PtA are, however, similar to that of the reference PtO₂. For M1PtA, the entire contributions arise only from Pt–O, Pt–O–Pt, and Pt–O–Al shells. This suggests atomic anchoring of Pt on the surface of alumina [41–45], which indicates strong interaction of Pt with Al₂O₃ and thereby supports the high stability of MPtA. For M3PtA, the higher

CNs of Pt–O and Pt–O–Pt shells are still obtained, while the Pt–Pt shell is found with the CN of 2.7 ± 0.6 much lower than those of *x*Pt/gA. This means the formation of Pt clusters, as seen in the HAADF-STEM image of M3PtA. However, the CN of Pt–Pt shell is measured to be 5.9 in M5PtA because of Pt nanoparticles.

Furthermore, CO-chemisorbed DRIFT spectra were taken for MPtA and Pt/gA catalysts. The spectra show different CO absorption bands in the MPtA and Pt/gA (Fig. 8a). In the spectra of *x*Pt/gA, the major CO stretching band is centered at 2060 cm^{-1}, representing metallic Pt nanoparticles [46–48]. In contrast, the CO stretching frequency is blueshifted for MPtA. M1PtA of Pt single atoms exhibits the CO stretching bands at 2083 and 2070 cm^{-1} with the background intensity at 2060 cm^{-1}. As the Pt loading increases, the former band is shifted to 2090 cm^{-1} as a result of the increase in Pt–Pt coordination number [41, 42]. Also, the CO stretching band at 2070 cm^{-1} becomes intense. This would be associated with linearly bound CO on Pt^0 clusters [41,42,49]. Therefore, the SDP method renders Pt species to be situated in the environment different from conventional Pt catalysts, although decisive comparison is hard.

Finally, H_2-TPD experiments were performed to understand the H_2 adsorption strength of Pt species. A low-temperature peak corresponds to weekly chemisorbed hydrogen on Pt (111) surface of Pt nanoparticles [50], as observed in the H_2-TPD profiles of *x*Pt/gA (Fig. 8b) and 1Pt/gA_B2 (Fig. S5b). In contrast, M1PtA exhibits H_2 desorption at 450 °C. A high-temperature peak is reported to be caused by strongly chemisorbed hydrogen on subsurface layers of Pt and Al₂O₃ [50]. This presumes that Pt single atoms and clusters in the MPtA have strong interactions with neighboring Al₂O₃ particles, explaining that the total amount of H_2 desorbed per gram Pt is larger for M*x*PtA than for *x*Pt/gA
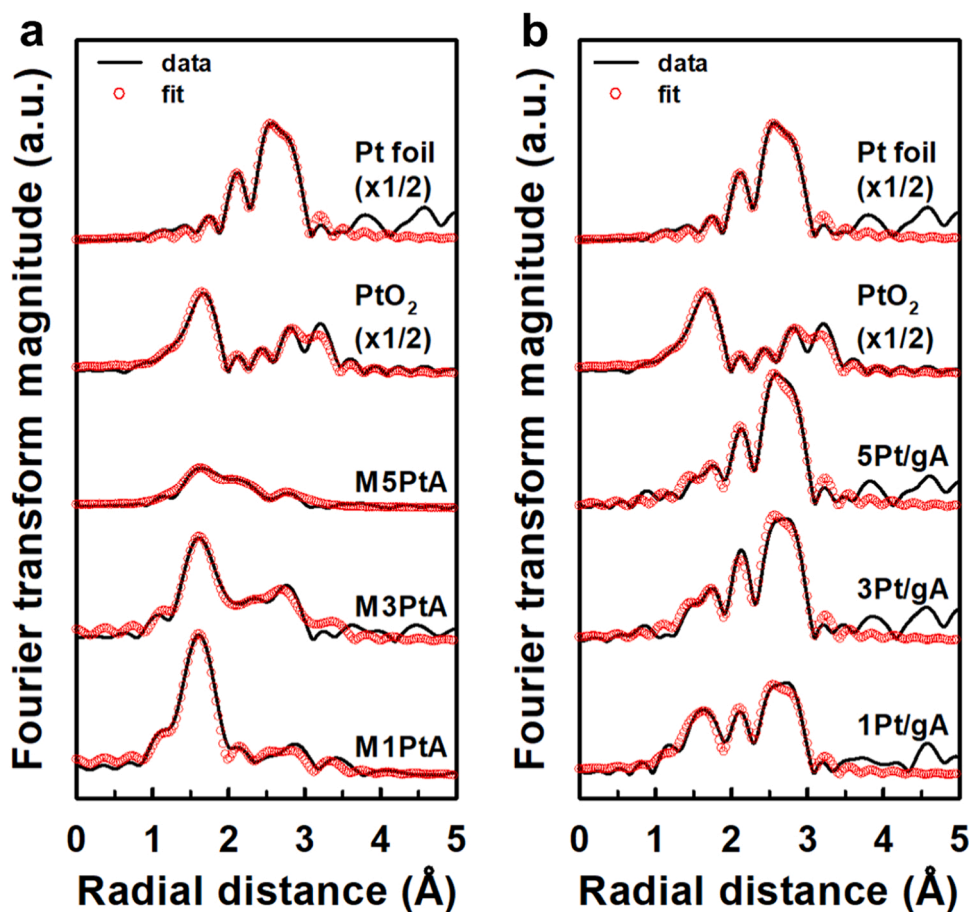

Fig. 7. Fourier transform k^3-weighted EXAFS oscillations of the prepared catalysts with the references Pt foil and PtO₂. (a) M*x*PtA. (b) *x*Pt/gA. (*x* = 1, 3, and 5 in a unit of wt%).
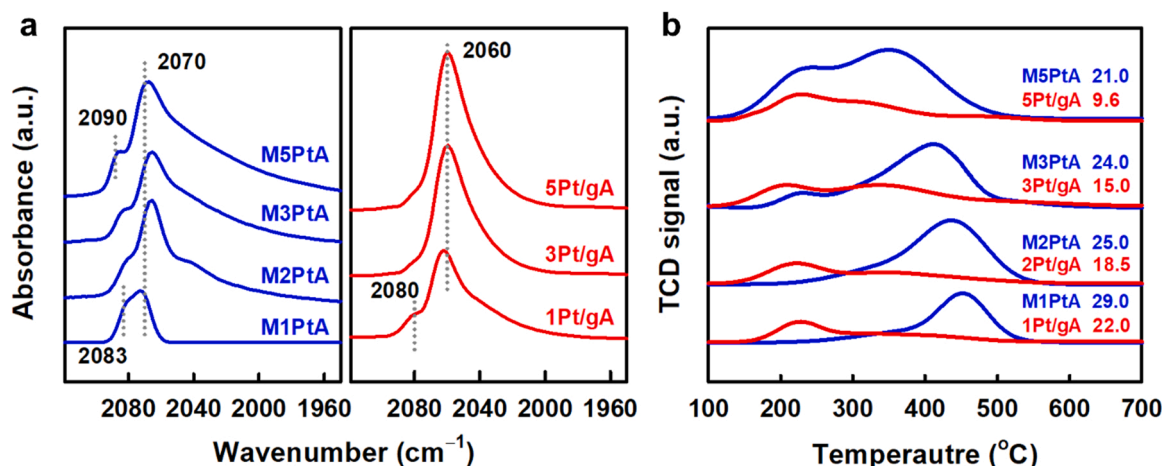
Fig. 8. Chemical features of the M*x*PtA (blue) and *x*Pt/gA (red) with the Pt loading (*x*) of 1, 2, 3, and 5 in a unit of wt%. (a) CO-chemisorbed DRIFT spectra. (b) H_2-TPD profiles. The values in panel b represents the total amounts of H_2 desorbed per gram Pt (unit: mmol g_{Pt}^{-1}).

at the same Pt loading. Also, such a peak is shifted to low temperature with the Pt loading increasing. Similarly, the low-temperature peaks with strong intensities are observed for the M1PtA_B2, M3PtA_B2, and M5PtA_B2 containing larger Pt species compared to the parent catalysts (Fig. S5b). Therefore, H_2 adsorption strength ranks in the following order: Pt nanoparticles < clusters < single atoms. Therefore, too strong H_2 adsorption of Pt single atoms is not favorable for both the dehydrogenation and hydrogenation reactions according to the Sabatier principle. That is, it hinders H_2 release from Pt surface in the former reaction and interferes the reactant adsorption by increased coverage of adsorbed hydrogen on Pt surface in the latter reaction. When this is combined with the larger H_2 adsorption of MPtA, Pt ensemble is expected to exhibit the best performance in the tested reactions.

4. Conclusions

The mesoporous Pt–Al_2O_3 catalyst showed extraordinary durability, and greater H_2 storage and release efficiencies for commercial LOHC molecules such as MBT and DBT. Thus, the MPtA achieved reversible interconversion between H_2-rich and H_2-lean MBT without catalyst deactivation. The employed SDP method is intriguingly unique to offer a broad range of Pt loading in producing single atoms as well as clusters to significantly affect the catalytic performance and product selectivity. Particularly, the best performance of M3PtA resulted from Pt ensembles of both single atoms and clusters, unlike the Pt/gA mainly composed of Pt nanoparticles. M3PtA was also robust because of the inhibited Pt growth by neighboring Al_2O_3 particles. This roots from the strong interaction of Pt and Al_2O_3 in the MPtA, as confirmed by EXAFS, CO-chemisorbed DRIFT, and H_2-TPD results. Therefore, the SDP method is capable of generating Pt single atoms and clusters in close proximity to surrounding alumina particles. Consequently, this work opens the potential synthesis approach to develop versatile Al_2O_3-supported metal catalysts of controlled size and arrangement for hydrogenation and dehydrogenation reactions demanding high power density.

CRediT authorship contribution statement

Jinho Oh: Investigation, Formal analysis, Data curation, Writing – original draft. **Yeongin Jo**: Investigation, Formal analysis, Data curation. **Tae Wan Kim:** Investigation, Formal analysis, Data curation. **Hari Babu Bathula:** Investigation, Formal analysis, Data curation. **Sungeun Yang:** Formal analysis, Data curation. **Joon Hyun Baik:** Formal analysis, Data curation. **Young-Woong Suh:** Conceptualization, Supervision, Funding acquisition, Writing – review & editing.

Declaration of Competing Interest

The authors declare that they have no known competing financial interests or personal relationships that could have appeared to influence the work reported in this paper.

Appendix A. Supporting information

Supplementary data associated with this article can be found in the online version at doi:10.1016/j.apcatb.2022.121061.

References

[1] A. Sartbaeva, V.L. Kuznetsov, S.A. Wells, P.P. Edwards, Hydrogen nexus in a sustainable energy future, Energy Environ. Sci. 1 (2008) 79–85.
[2] S.S. Penner, Steps toward the hydrogen economy, Energy 31 (2006) 33–43.
[3] R.J. Detz, J.N.H. Reek, B.C.C. van der Zwaan, The future of solar fuels: when could they become competitive, Energy Environ. Sci. 11 (2018) 1653–1669.
[4] G.W. Crabtree, M.S. Dresselhaus, M.V. Buchanan, The hydrogen economy, Phys. Today 57 (2004) 39–44.
[5] M. Niermann, S. Drünert, M. Kaltschmitt, K. Bonhoff, Liquid organic hydrogen carriers (LOHCs) – techno-economic analysis of LOHCs in a defined process chain, Energy Environ. Sci. 12 (2019) 290–307.
[6] P. Preuster, C. Papp, P. Wasserscheid, Liquid organic hydrogen carriers (LOHCs): toward a hydrogen-free hydrogen economy, Acc. Chem. Res. 50 (2017) 74–85.
[7] M. Niermann, S. Timmerberg, S. Drünert, M. Kaltschmitt, Liquid organic hydrogen carriers and alternatives for international transport of renewable hydrogen, Renew. Sustain. Energy Rev. 135 (2021), 110171.
[8] M. Niermann, A. Beckendorff, M. Kaltschmitt, K. Bonhoff, Liquid organic hydrogen carrier (LOHC) – assessment based on chemical and economic properties, Int. J. Hydrog. Energy 44 (2019) 6631–6654.
[9] M. Markiewicz, Y.Q. Zhang, A. Bösmann, N. Brückner, J. Thöming, P. Wasserscheid, S. Stolte, Environmental and health impact assessment of liquid organic hydrogen carrier (LOHC) systems – challenges and preliminary results, Energy Environ. Sci. 8 (2015) 1035–1045.
[10] S. Lee, T. Kim, G. Han, S. Kang, Y.-S. Yoo, S.-Y. Jeon, J. Bae, Comparative energetic studies on liquid organic hydrogen carrier: a net energy analysis, Renew. Sustain. Energy Rev. 150 (2021), 111447.
[11] P.M. Modisha, C.N.M. Ouma, R. Garidzirai, P. Wasserscheid, D. Bessarabov, The prospect of hydrogen storage using liquid organic hydrogen carriers, Energy Fuels 33 (2019) 2778–2796.

[12] H. Wang, X. Zhou, M. Ouyang, Efficiency analysis of novel liquid organic hydrogen carrier technology and comparison with high pressure storage pathway, Int. J. Hydrog. Energy 41 (2016) 18062–18071.

[13] N. Brückner, K. Obesser, A. Bösmann, D. Teichmann, W. Arlt, J. Dungs, P. Wasserscheid, Evaluation of industrially applied heat-transfer fluids as liquid organic hydrogen carrier systems, ChemSusChem 7 (2014) 229–235.

[14] H. Jorschick, M. Geißelbrecht, M. Eßl, P. Preuser, A. Bösmann, P. Wasserscheid, Benzyltoluene/dibenzyltoluene-based mixtures as suitable liquid organic hydrogen carrier systems for low temperature applications, Int. J. Hydrog. Energy 45 (2020) 14897–14906.

[15] L. Shi, Y. Zhou, S. Qi, K.J. Smith, X. Tan, J. Yan, C. Yi, Pt catalysts supported on H$_2$ and O$_2$ plasma-treated Al$_2$O$_3$ for hydrogenation and dehydrogenation of the liquid organic hydrogen carrier pair dibenzyltoluene and perhydrodibenzyltoluene, ACS Catal. 10 (2020) 10661–10671.

[16] W. Peters, M. Eypasch, T. Frank, J. Schwerdtfeger, C. Körner, A. Bösmann, P. Wasserscheid, Efficient hydrogen release from perhydro-N-ethylcarbazole using catalyst-coated metallic structures produced by selective electron beam melting, Energy Environ. Sci. 8 (2015) 641–649.

[17] J. Oh, K. Jeong, T.W. Kim, H. Kwon, J.W. Han, J.H. Park, Y.-W. Suh, 2-(N-methylbenzyl)pyridine: a potential liquid organic hydrogen carrier with fast H$_2$ release and stable activity in consecutive cycles, ChemSusChem 11 (2018) 661–665.

[18] M. Geißelbrecht, S. Mrusek, K. Müller, P. Preuser, A. Bösmann, P. Wasserscheid, Highly efficient, low-temperature hydrogen release from perhydro-benzyltoluene using reactive distillation, Energy Environ. Sci. 13 (2020) 3119–3128.

[19] F. Sotoodeh, B.J.M. Huber, K.J. Smith, Dehydrogenation kinetics and catalysis of organic heteroaromatics for hydrogen storage, Int. J. Hydrog. Energy 37 (2012) 2715–2722.

[20] B. Wang, Y.-T. Chen, T.-Y. Chang, Z. Jiang, Z.-Q. Huang, S.-Y. Wang, C.-R. Chang, Y.-S. Chen, J.-J. Wei, S. Yang, T. Fang, Facet-dependent catalytic activities of Pd/rGO: exploring dehydrogenation mechanism of dodecahydro-N-ethylcarbazole, Appl. Catal. B 266 (2020), 118658.

[21] J. Oh, H.B. Bathula, J.H. Park, Y.-W. Suh, A sustainable mesoporous palladium-alumina catalyst for efficient hydrogen release from N-heterocyclic liquid organic hydrogen carriers, Commun. Chem. 2 (2019) 68.

[22] H.B. Bathula, J. Oh, Y. Jo, Y.-W. Suh, Dehydrogenation of 2-[(n-methylcyclohexyl) methyl]piperidine over mesoporous Pd-Al$_2$O$_3$ catalysts prepared by solvent deficient precipitation: influence of calcination conditions, Catalysts 9 (2019) 719.

[23] J. Gao, H. Zhao, X. Yang, B.E. Koel, S.G. Podkolzin, Geometric requirements for hydrocarbon catalytic sites on platinum surfaces, Angew. Chem. Int. Ed. 53 (2014) 3641–3644.

[24] R.H. Crabtree, Hydrogen storage in liquid organic heterocycles, Energy Environ. Sci. 1 (2008) 134–138.

[25] P. Modisha, D. Bessarabov, Stress tolerance assessment of dibenzyltoluene-based liquid organic hydrogen carriers, Sustain. Energy Fuels 4 (2020) 4662–4670.

[26] F. Auer, D. Blaumeiser, T. Bauer, A. Bösmann, N. Szesni, P. Wasserscheid, Boosting the activity of hydrogen release from liquid organic hydrogen carrier systems by sulfur-additives to Pt on alumina catalysts, Catal. Sci. Technol. 9 (2019) 3537–3547.

[27] F. Auer, A. Hupfer, A. Bösmann, N. Szesni, P. Wasserscheid, Influence of the nanoparticle size on hydrogen release and side product formation in liquid organic hydrogen carrier systems with supported platinum catalysts, Catal. Sci. Technol. 10 (2020) 6669–6678.

[28] A. Nakano, S. Manabe, T. Higo, H. Seki, S. Nagatake, T. Yabe, S. Ogo, T. Nagatsuka, Y. Sugiura, H. Iki, Y. Sekine, Effects of Mn addition on dehydrogenation of methylcyclohexane over Pt/Al$_2$O$_3$ catalyst, Appl. Catal. A 543 (2017) 75–81.

[29] N. Boufaden, R. Akkari, B. Pawelec, J.L.G. Fierro, M.S. Zina, A. Ghorbel, Dehydrogenation of methylcyclohexane to toluene over partially reduced silica-supported Pt-Mo catalysts, J. Mol. Catal. A 420 (2016) 96–106.

[30] S. Yang, J. Kim, Y.J. Tak, A. Soon, H. Lee, Single-atom catalyst of platinum supported on titanium nitride for selective electrochemical reactions, Angew. Chem. Int. Ed. 55 (2016) 2058–2062.

[31] Z. Zhang, Y. Zhu, H. Asakura, B. Zhang, J. Zhang, M. Zhou, Y. Han, T. Tanaka, A. Wang, T. Zhang, N. Yan, Thermally stable single atom Pt/m-Al$_2$O$_3$ for selective hydrogenation and CO oxidation, Nat. Commun. 8 (2017) 16100.

[32] L. DeRita, S. Dai, K. Lopez-Zepeda, N. Pham, G.W. Graham, X. Pan, P. Christopher, Catalyst architecture for stable single atom dispersion enables site-specific spectroscopic and reactivity measurements of CO adsorbed to Pt atoms, oxidized Pt clusters, and metallic Pt clusters on TiO$_2$, J. Am. Chem. Soc. 139 (2017) 14150–14165.

[33] T.W. Kim, M. Kim, S.K. Kim, Y.N. Choi, M. Jung, H. Oh, Y.-W. Suh, Remarkably fast low-temperature hydrogen storage into aromatic benzyltoluenes over MgO-supported Ru nanoparticles with homolytic and heterolytic H$_2$ adsorption, Appl. Catal. B 286 (2021), 119889.

[34] K. Müller, K. Stark, V.N. Emel'yanenko, M.A. Varfolomeev, D.H. Zaitsau, E. Shoifet, C. Schick, S.P. Verevkin, W. Arlt, Liquid organic hydrogen carriers: thermophysical and thermochemical studies of benzyl- and dibenzyl-toluene derivatives, Ind. Eng. Chem. Res. 54 (2015) 7967–7976.

[35] L. Shi, S. QI, J. QU, T. Che, C. Yi, B. Yang, Integration of hydrogenation and dehydrogenation based on dibenzyltoluene as liquid organic hydrogen energy carrier, Int. J. Hydrog. Energy 44 (2015) 5345–5354.

[36] H. Itoi, H. Nishihara, S. Kobayashi, S. Ittisanronnachai, T. Ishii, R. Berenguer, M. Ito, D. Matsumura, T. Kyotani, Fine dispersion of Pt$_{4-5}$ subnanoclusters and Pt single atoms over porous carbon supports and their structural analyses with X-ray absorption spectroscopy, J. Phys. Chem. C 121 (2017) 7892–7902.

[37] H. Rong, S. Ji, J. Zhang, D. Wang, Y. Li, Synthetic strategies of supported atomic clusters for heterogeneous catalysis, Nat. Commun. 11 (2020) 5884.

[38] Q.-Q. Yan, D.-X. Wu, S.-Q. Chu, Z.-Q. Chen, Y. Lin, M.-X. Chen, J. Zhang, X.-J. Wu, H.-W. Liang, Reversing the charge transfer between platinum and sulfur-doped carbon support for electrocatalytic hydrogen evolution, Nat. Commun. 10 (2019) 4977.

[39] Y. Qiu, Z. Wen, C. Jiang, X. Wu, R. Si, J. Bao, Q. Zhang, L. Gu, J. Tang, X. Guo, Rational design of atomic layers of Pt anchored on Mo$_2$C nanorods for efficient hydrogen evolution over a wide pH range, Small 15 (2019) 1900014.

[40] M.D. Rossell, F.J. Caparrós, I. Angurell, G. Muller, J. Llorca, M. Seco, O. Rossell, Magnetite-supported palladium single-atoms do not catalyse the hydrogenation of alkenes but small clusters do, Catal. Sci. Technol. 6 (2016) 4081–4085.

[41] J. Kim, H.-E. Kim, H. Lee, Single-atom catalysts of precious metals for electrochemical reactions, ChemSusChem 11 (2018) 104–113.

[42] H.J. Kale, P. Christopher, Utilizing quantitative in situ FTIR spectroscopy to identify well-coordinated Pt atoms as the active site for CO oxidation on Al$_2$O$_3$-supported Pt catalysts, ACS Catal. 6 (2016) 5599–5609.

[43] H. Wei, X. Liu, A. Wang, L. Zhang, B. Qiao, X. Yang, Y. Huang, S. Miao, J. Liu, T. Zhang, FeO$_x$-supported platinum single-atom and pseudo-single-atom catalysts for chemoselective hydrogenation of functionalized nitroarenes, Nat. Commun. 5 (2014) 5634.

[44] N. Cheng, S. Stambula, D. Wang, M.N. Banis, J. Liu, A. Riese, B. Xiao, R. Li, T.-K. Sham, L.-M. Liu, G.A. Botton, X. Sun, Platinum single-atom and cluster catalysis of the hydrogen evolution reaction, Nat. Commun. 7 (2016) 13638.

[45] Z. Zhang, Y. Zhu, H. Asakura, B. Zhang, J. Zhang, M. Zhou, Y. Han, T. Tanaka, A. Wang, T. Zhang, N. Yan, Thermally stable single atom Pt/m-Al$_2$O$_3$ for selective hydrogenation and CO oxidation, Nat. Commun. 8 (2017) 16100.

[46] D.N. McCarthy, C.E. Strebel, T.P. Johansson, A. den Dunnen, A. Nierhoff, J. H. Nielsen, I. Chorkendorff, Structural modification of platinum model systems under high pressure CO annealing, J. Phys. Chem. C 116 (2012) 15353–15360.

[47] K. Ding, A. Gulec, A.M. Johnson, N.M. Schweitzer, G.D. Stucky, L.D. Marks, P. C. Stair, Identification of active sites in CO oxidation and water-gas shift over supported Pt catalysts, Science 350 (2015) 189–192.

[48] H. Jeong, D. Shin, B.-S. Kim, J. Bae, S. Shin, C. Choe, J.W. Han, H. Lee, Controlling the oxidation state of Pt single atoms for maximizing catalytic activity, Angew. Chem. 132 (2020) 20872–20877.

[49] D. Yan, J. Chen, H. Jia, Temperature-induced structure reconstruction to prepare a thermally stable single-atom platinum catalyst, Angew. Chem. Int. Ed. 59 (2020) 13562–13567.

[50] J.T. Miller, B.L. Meyers, F.S. Modica, G.S. Lane, M. Vaarkamp, D.C. Koningsberger, Hydrogen temperature-programmed desorption (H$_2$ TPD) of supported platinum catalysts, J. Catal. 143 (1993) 395–408.